

Directional drying of a colloidal dispersion: quantitative description with water potential measurements using water clusters in a poly(dimethylsiloxane) microfluidic chip

Hrishikesh Pingulkar,¹ Sonia Maréchal,¹ and Jean-Baptiste Salmon¹
 CNRS, Solvay, LOF, UMR 5258, Université de Bordeaux, 178 av. Schweitzer, Pessac,
 33600

(Dated: 11 January 2024)

We have developed a poly(dimethylsiloxane) (PDMS) microfluidic chip to study the directional drying of a colloidal dispersion confined in a channel. Our measurements on a dispersion of silica nanoparticles once again revealed the phenomenology commonly observed for such systems: the formation of a porous solid with linear growth in the channel at short times, slowing down at longer times as the evaporation rate decreases. The growth of the solid is also accompanied by mechanical stresses that are released by the delamination of the solid from the channel walls and the formation of cracks. In addition to these observations, we report original measurements using hydrophilic filler in the PDMS formulation used (Sylgard-184). When the PDMS matrix is in contact with water, water molecules pool around these hydrophilic sites, resulting in the formation of microscopic water clusters whose size depends on the water potential ψ . In our work, we have used these water clusters to estimate the water potential profile in the channel as the porous solid grows. Using a transport model that also takes into account solid delamination in the channel, we then linked these water potential measurements to the hydraulic permeability of the porous solid. These measurements finally enabled us to show that the slowdown in the evaporation rate is due to the invasion of the porous solid by air/water nanomenisci at a critical capillary pressure ψ_{cap} .

I. INTRODUCTION

The drying of colloidal dispersions, a common step in many manufacturing processes, remains a fascinating subject of study whose understanding involves many aspects from the physico-chemistry of colloids, transport phenomena, to the mechanics of porous solids¹⁻⁴. For a general understanding of these phenomena, many groups have focused on model cases, such as the confined directional drying⁵⁻⁷. In such experiments, a dilute dispersion is confined within a capillary or Hele-Shaw cell, with cross-sectional dimensions $< 100 \mu\text{m}$, see Fig. 1a for a schematic view. When the air/dispersion meniscus is pinned at the outlet of the cell, solvent evaporation induces a flow at a rate J (m/s) due to mass conservation. This flow then accumulates the colloids at the end of the cell until a consolidated solid is formed. For rigid colloids, the porosity of the solid does not stop solvent evaporation, even for nanoparticles as small as a few nm^{6,7}, and the solid invades the cell at a rate \dot{x}_c . At longer times, the evaporation-induced flow through the porous solid leads to mechanical stresses that are released by instabilities: formation of shear bands⁸⁻¹⁰, delamination of the solid from the cell walls^{11,12}, and formation of cracks^{5,6,13-15}.

Confined directional drying has been used in many studies to better understand the drying of colloidal dispersions, from the mechanical instabilities mentioned above to transport phenomena¹⁶⁻²¹. This is mainly due to the control of evaporation conditions in this one-dimensional drying geometry and the monitoring possibilities offered by this technique. In addition to these studies, confined directional drying is also a model configuration for studying the drying of porous media saturated with a colloidal dispersion in the capillary regime^{22,23}. Despite all these studies, the evaporation kinetics, J vs t , and the growth of the porous solid, x_c vs t , remain open questions

to this day²⁴. In the case of nanoparticles with typical radii $a \leq 20 \text{ nm}$, experiments have shown that the solid layer first grows linearly, $x_c \sim t$, and then follows a square root growth $x_c \sim t^{0.5}$ indicating a decrease of the evaporation-induced flow rate J ^{6,11,14,25}. Most theoretical works suggest that this slowdown is actually due to the minute recession of the evaporation interface within the porous solid, adding a high resistance to evaporation linked to the diffusion of water vapour in the dry porous layer, the so-called *capillary-limited regime*^{7,24-26}. For very small colloids ($a < 10 \text{ nm}$), the water pore pressure at the evaporation interface can decrease down to values that affect the partial pressure of water in the gas phase, the so-called Kelvin effect²⁷. In this *flow-limited regime*, there is no resistance to evaporation in the gas phase, and the slowdown is explained by the increasing resistance due to the flow through the growing porous solid²⁴. To date, no work has been done to differentiate experimentally between these two regimes (except ref.²⁸, but for drying-induced permeation in nanoporous media), nor has quantitative modelling been carried out, due to the lack of data describing the porous solid, in particular its hydraulic permeability κ (m²). Furthermore, all the theoretical studies are based on one-dimensional modelling of transport phenomena, and do not take into account the possible role played by cracks and solid delamination on the solvent evaporation.

Our aim in the present work is to bring new insights on the confined directional drying of a dispersion of silica nanoparticles (mean radius $a = 11 \text{ nm}$), using experiments in a poly(dimethylsiloxane) (PDMS) microfluidic chip. Our experiments first enable the directional drying of the colloidal dispersion in a highly confined geometry (cross-section $h \times w = 30 \times 100 \mu\text{m}^2$, see Fig. 1), while providing accurate measurements of both the evaporation kinetics J vs t , and the growth rate of the solid, x_c vs t . We also exploit the pres-

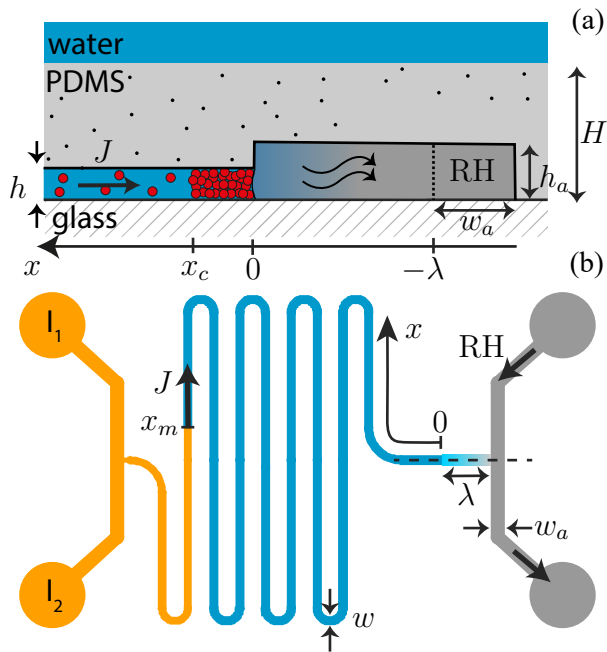


FIG. 1. (a) Sketch of confined directional drying of a colloidal dispersion, and cross-sectional view along the dashed line of the microfluidic chip shown in (b). Dimensions: $h = 30$, $h_a = 70$, $w_a = 300$, $\lambda = 500$, and $H \simeq 200 \mu\text{m}$. The water bath on top of the PDMS layer prevents pervaporation. Colloids are shown in red, with black dots representing the water clusters in PDMS, see Section III B. (b) Schematic view of the microfluidic chip. Blue indicates water, yellow fluorinated oil. I_1 and I_2 are the two liquid inlets. Air flows at a controlled relative humidity RH in the gray channel (width w_a). Evaporation induces a flow at a rate $J = -\dot{x}_m$ in the main channel ($w = 100 \mu\text{m}$) as long as the air/water meniscus remains pinned at $x = 0$.

ence of hydrophilic filler in the PDMS formulation used, to estimate the water potential ψ (Pa) along the porous solid as it grows. These original data, combined with a model taking into account the presence of an air film linked to delamination, enable us to estimate the permeability κ of the porous solid and show that the slowdown observed in our configuration corresponds to the *capillary-limited regime*.

The present paper is organized as follows. In Section II, we present the microfluidic tools used and the experimental methods employed. In Section III, we present the main results of our work, in particular concerning the confined directional drying of a nanoparticle dispersion and its quantitative description. In Section IV, we conclude our work and suggest various perspectives.

II. MATERIALS AND METHODS

A. A PDMS chip for confined directional drying

Fig. 1 shows schematically the chip we designed to study the confined directional drying of colloidal dispersions. We used standard soft lithography techniques to fabricate this chip

with Sylgard-184 PDMS (mass ratio curing agent/polymeric base = 1/10). The channel network is composed of two inlets (I_1 and I_2) connected to a serpentine-like channel of length $L = 43 \text{ mm}$, and height \times width $h \times w = 30 \times 100 \mu\text{m}^2$. The latter leads to a higher channel (height $h_a = 70 \mu\text{m}$) in which air at an imposed relative humidity (RH) flows. The height step in the channel ($h \rightarrow h_a$) helps to trap an air/water meniscus when an aqueous colloidal dispersion is injected using either inlet I_1 or I_2 ^{29,30}. Water evaporation from the air/water meniscus then drives a flow at a rate J as long as the meniscus remains trapped, accumulating the colloids up to the formation of a porous solid that finally invades the channel. Many similar microfluidic experiments have been carried out, particularly in the context of passive pumping^{31,32} or for evaporative assembly of colloidal materials^{29,30}, see ref.³³ for a review.

In the absence of colloids, the evaporation rate under isothermal conditions can be estimated by^{31–33}:

$$J = \frac{k c_{\text{sat}}}{\rho_w} (1 - RH), \quad (1)$$

with c_{sat} (kg/m^3) the saturation vapor concentration in air, ρ_w (kg/m^3) the mass density of liquid water, and k (m/s) a mass transport coefficient. For diffusion-dominated transport for the water vapour over the length scale λ (see Fig. 1), $k \simeq (h_a/h) D_w^{\text{air}}/\lambda$ with D_w^{air} ($\text{m}^2 \text{s}^{-1}$), the diffusion coefficient of the water vapour in air³⁴. Eqn (1) leads to evaporation rates ranging from $J \simeq 0.5$ to $2.3 \mu\text{m s}^{-1}$ for relative humidity ranging from $RH = 0.8$ to 0 . However, the PDMS matrix is not totally impermeable to water, as water molecules can solubilize in the elastomer, diffuse, and then evaporate into the ambient air, a mechanism known as pervaporation. Water pervaporation in our PDMS chip inevitably leads to a flow directed towards the fixed air/water meniscus^{35,36}, and thus superimposed on the flow induced by evaporation. This pervaporation-induced flow can in turn also concentrate the colloids as in the many applications reviewed in Ref.³³. Dollet et al. calculated the flow due to pervaporation for a single linear channel of rectangular cross-section³⁷. This relation leads to an estimated pervaporation-induced flow $J_p \simeq 6 \mu\text{m s}^{-1}$ for the filled serpentine channel shown in Fig. 1, $H = 200 \mu\text{m}$, and an external relative humidity $RH = 0.5$. This flow, significantly larger than the evaporation-induced flow predicted by eqn (1), can be reduced by increasing H , but not completely³³. Indeed, for the serpentine channel, the assumption of a single linear channel no longer holds for large H , but theoretical estimates in this case³⁸ still lead to $J_p \simeq 0.1\text{--}1 \mu\text{m s}^{-1}$ for thicknesses H of a few mm. Hence, in order to fully neglect pervaporation in our work, the whole chip is immersed in water before and during the experiments, as demonstrated in ref.³⁵. With this simple technique, the pervaporation-induced flows are fully eliminated after a time scale of the order of $\tau_p \simeq H^2/D_w^p$, $D_w^p \simeq 6\text{--}8 \times 10^{-10} \text{ m}^2 \text{ s}^{-1}$ being the diffusion coefficient of water in PDMS³³. This led us to choose a thickness $H \simeq 200 \mu\text{m}$ for our experiments, a compromise between the time required to stop pervaporation, τ_p of the order of a few minutes in this case, and the limits of microfabrication of thin PDMS chips.

B. Confined directional drying experiments

We studied a charge-stabilized dispersion of silica nanoparticles in water commercialized under the name Ludox AS40 (monodisperse anionic grade, Sigma Aldrich). The volume fraction of the commercial dispersion estimated using dry extract measurements is $\phi_0 \simeq 0.24$ and the mean radius of the nanoparticles is $a = 11 \text{ nm}$ ³⁹. All experiments were carried out at room temperature, $T \simeq 22^\circ\text{C}$.

In a typical experiment, the microfluidic chip is first immersed in a water bath for about 1 h, and an air stream of controlled RH is imposed in the air channel (typical rate 0.4 mL min^{-1} , HumiSys LF RH generator, InstruQuest Inc.). Then, the dispersion of silica nanoparticles is injected in the chip through inlet I_1 using a small amount of excess pressure (typically 50 mbar, MFCS, Fluigent). The dispersion invades the main channel and the geometric step traps the air/dispersion meniscus ($x = 0$). Then, a fluorinated oil (Fluorinert FC40, 3M) is gently injected from inlet I_1 towards I_2 , leading to the formation of an oil/dispersion meniscus at $x_m = L$, the inlet of the serpentine channel. This is only possible because our device has two inlets, I_1 and I_2 , connected to the same main channel. Finally, we used bright field microscopy (Olympus IX73) at 2X magnification (spatial resolution $3.25 \mu\text{m}/\text{pixel}$) using a sCMOS camera (Orca 4, Hamamatsu) to track both the drying process along the channel and estimate the evaporation-induced flow rate from the displacement of the oil/dispersion meniscus by :

$$J = -\frac{dx_m}{dt}. \quad (2)$$

C. Raman microscopy

The confocal Raman measurements shown in Section III B were obtained with a custom-made Raman microspectrometer setup coupled to an inverted microscope (Olympus IX71). A laser beam (wavelength 532 nm, output power $\simeq 30 \text{ mW}$) is focused with a water-immersion 60X objective (NA of 1.2) on the water clusters observed in the PDMS film and discussed in Section III B. The scattered light is collected by the same objective, filtered, and directed to the spectrometer (Andor Shamrock, grating $600 \text{ lines mm}^{-1}$, input slit width $100 \mu\text{m}$). A confocal pinhole ($100 \mu\text{m}$) reduces the out-of-focus contributions. Typical acquisition times were of the order of 2 s.

III. RESULTS

A. Confined directional drying, global views

Fig. 2 shows a snapshot at $t = 100 \text{ min}$ of the confined directional drying of the dispersion of silica nanoparticles for an experiment performed with an air stream of relative humidity $\text{RH} = 0.2$, see the movies M1.avi and M2.avi †. For the sake of clarity, this snapshot zooms on the first turn in the serpentine channel, but the full field of view makes it possible

to visualize the oil/dispersion meniscus and thus measure the evaporation rate J using eqn (2).

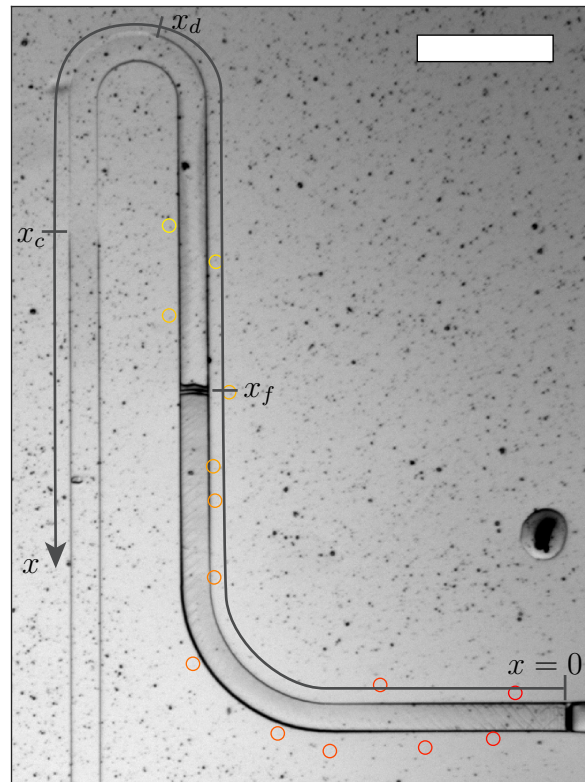


FIG. 2. Snapshot at $t = 100 \text{ min}$ zooming on the first turn in the serpentine channel, see also movie M2.avi †. x_c indicates the compaction front, x_d the delamination front, and x_f the position of the single crack at that instant. The scale bar is equal to $500 \mu\text{m}$. The colored circles surround the positions of the water clusters in PDMS that are used to estimate the water potential, see Section III B and Fig. 7 (they have almost all disappeared at $t = 100 \text{ min}$). Their colors, from red to yellow, indicate their increasing positions x_i from the end of the channel, see the axis.

Our observations once again reveal the phenomenology commonly observed during the confined directional drying of such dispersions^{6,7,25}. At initial times, the accumulation of the nanoparticles at $x = 0$, leads to the formation of a porous solid which then invades the main channel, as it is constantly fed by an evaporation-induced flux of colloids. A compaction front separates the dilute dispersion from this colloidal material. Its position x_c is easily identified by the disappearance of the channel walls, due to the matching of the optical indices of the PDMS and the dispersion at the compaction front. This transition from a liquid dispersion to a solid is accompanied by the onset of mechanical stresses^{26,40}. In our case, these stresses deform the microfluidic channel, until the colloidal solid detaches from it, as often reported for similar experiments^{11,12}. The delamination front, denoted x_d , broadly follows the compaction front but intermittently, and is easily detected thanks to the strong optical contrast associated with the formation of an air film. In the experiment, see Fig. 2, the

solid initially detaches from the vertical walls of the channel, then later across its entire width. Subsequently, these mechanical stresses cause cracks to form in the colloidal solid, as also observed many times for similar experiments^{5,6,13,14}, but with specific characteristics linked to the high confinement of the channel. The number of cracks is indeed relatively limited (3 in the experiment presented at $t = 500$ min), and they are transverse to the porous solid, literally cutting it into several distinct pieces. Even at 2X magnification, our observations also revealed the presence of shear bands in the growing solid, as often described in similar experiments^{8–10}.

Fig. 3a gathers the tracking of both the compaction and delamination fronts, x_c and x_d respectively, along with the positions x_f of the cracks when they appear. Initially, the compaction front grows linearly along the channel, $x_c \sim t$, and then slows down for $t \gtrsim 80$ min following at long time scale $x_c \sim t^\alpha$, with $\alpha \simeq 0.4$. This smooth growth does not seem to be affected by the intermittent dynamics of the delamination front, nor by the sudden appearance of cracks. In addition, other experiments carried out under the same conditions led to very similar observations for x_c vs t , but with noticeable differences for the delamination front and the number and positions of the cracks, consistently with the stochastic nature of these phenomena.

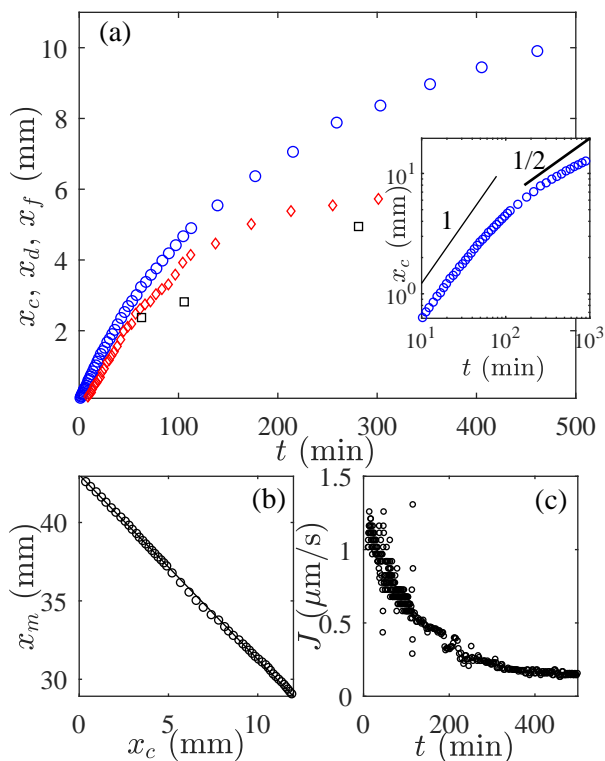


FIG. 3. (a) Compaction front x_c (\circ), delamination front x_d (\diamond) and positions of cracks x_f as they appear (\square) as a function of time t . Inset: x_c vs t in log-log scale. (b) Position of the meniscus x_m against the compaction front x_c . The continuous line is a linear fit. (c) Evaporation rate J estimated from the displacement of the meniscus using eqn (2).

Fig. 3b shows the position of the oil/dispersion meniscus

x_m , versus the compaction front x_c . The relationship between these two quantities is affine, and linked to the colloid conservation as discussed later. Finally, Fig. 3c shows the evaporation rate J estimated from eqn (2) as a function of time. This curve shows that J decreases continuously from $J \simeq 1.3 \mu\text{m s}^{-1}$ to around $J \simeq 100 \text{ nm s}^{-1}$ at long times. All the observations described above, as well as the values of the dynamics x_c vs t and J vs t shown in Fig. 3 are consistent with published data for similar experiments^{6,7,11,14}, see in particular ref.²⁵. On the other hand, it is important to point out that our data suggest a slowdown at long times following $x_c \sim t^\alpha$, with an exponent $\alpha \simeq 0.4$ slightly lower than the 0.5 value often reported in the references cited above. Although it is always tricky to estimate such exponent from fits over small time ranges, we believe that this over-slowdown is significant and possibly due to the permeation of water from the reservoir on top of the PDMS chip towards the channel, as discussed in Section III F.

B. Water clusters in PDMS

In addition to the observations described above, our experiments revealed a new phenomenon. When the chip is immersed in the water bath, a large number of small inclusions appear in the PDMS, absorbing or scattering light, therefore suggesting impurities, see the black dots on Fig. 2. Local observations at higher magnifications show that these inclusions are highly dispersed, with sizes ranging from fractions of a micron to nearly $10 \mu\text{m}$ for the largest. When the chip is removed from the water bath, these inclusions disappear, and the PDMS becomes completely transparent again. As shown in Fig. 4a, the inclusions appear again exactly at the same positions as before when the chip is re-immersed in water, suggesting the presence of preferential sites within the PDMS matrix. Confocal Raman spectroscopy measurements on these inclusions revealed the OH stretching vibrations of the water molecules, suggesting that they are in fact microscopic water clusters, see Fig. 4b and 4c.

Such observations are not new, as silicone elastomers are known to become milky when immersed in water, due to the formation of water clusters that scatter light. The origin of these clusters is actually linked to the presence in the matrix of hydrophilic sites, either impurities or filler materials, which can significantly absorb water molecules⁴¹. In the case of Sylgard-184, the poly(dimethylsiloxane) used in the present study, these sites are probably silica filler with high specific surface area, added to the commercial blend by the manufacturer to improve the mechanical properties of the elastomer⁴². Harley et al. have measured the role of these hydrophilic sites on the equilibrium sorption of water vapour in cross-linked Sylgard-184⁴². For low water vapour activity ($\text{RH} < 0.1$), these sites allow the immobilization of water molecules via Langmuir-type adsorption, whereas the sorption of water increases drastically at higher water vapour activity, $\text{RH} > 0.7$ – 0.8 . These authors attributed this effect to the clustering of the water molecules around the Langmuir sites. These results led us to the possibility that the water clusters we observe are also

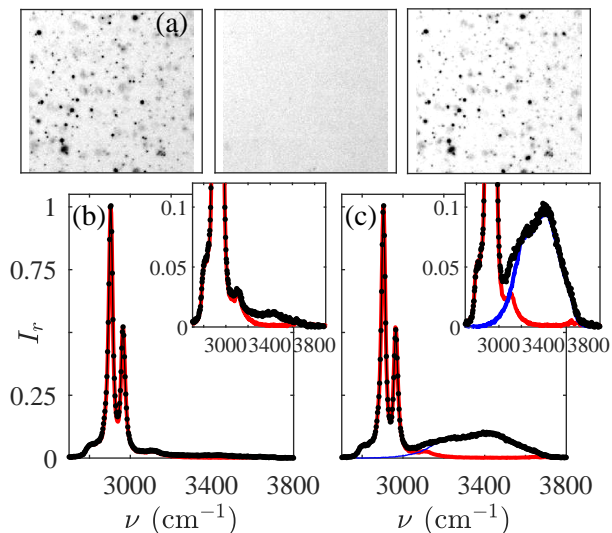


FIG. 4. (a) Images ($325 \times 325 \mu\text{m}^2$) of a PDMS layer $200 \mu\text{m}$ thick, which, from left to right, is first immersed in a water bath, then removed and exposed to ambient air, before being immersed again in the water bath. (b) and (c): Raman spectra (\cdot) measured at the position of a water cluster in a PDMS film in (b) ambient air and (c) when immersed in water. Both spectra are normalized by the Raman peak at $\nu \simeq 2900 \text{ cm}^{-1}$ due to the PDMS matrix. The red curves correspond to the Raman spectrum of PDMS measured in a cluster-free region, and blue curves to the spectrum of water. The insets show zooms on the OH stretching vibrations in the spectral range $\nu = [3000\text{--}3800] \text{ cm}^{-1}$.

sensitive to the water activity a_w in which the PDMS is immersed, and thus on the water potential $\psi = RT/V_m \log(a_w)$, with $V_m \simeq 1.805 \times 10^{-5} \text{ m}^3 \text{ mol}^{-1}$, the liquid water molar volume at room temperature ($T = 22^\circ\text{C}$), and R the universal gas constant.

Fig. 5a shows the experiments we did for testing this assumption. A thin PDMS film is coated on a glass slide, and we added a wide channel ($\simeq 1 \text{ mm}$ in width, $\simeq 200 \mu\text{m}$ in height) on top to inject aqueous solutions of known water potential, binary mixtures water/NaCl (at molalities up to 5 mol/kg)⁴³ and water/glycerol (at glycerol mass fractions up to 0.6)^{44,45}. For $\psi \leq -40 \text{ MPa}$ ($a_w \leq 0.75$), we do not observe any water clusters at the magnification 10X, while the clusters grow in size when the water potential increases up to $\psi = 0$ ($a_w = 1$, pure water). For this thickness of PDMS layer, $\simeq 20 \mu\text{m}$, we did not observe any kinetic effect as the appearance or disappearance of the clusters follows the imposed water potential almost instantaneously. To quantify more precisely these observations, we averaged the light intensity collected by the camera over a few microns around several clusters, then subtracted the intensity measured in a cluster-free region to eliminate the fluctuations of the illumination. This quantity is finally normalized between 0 and 1 and plotted in Fig. 5b against ψ . Despite the errorbars, mainly due to the dispersity of the observed inclusions, these measurements show that the water clusters are indeed sensitive to the water potential, as

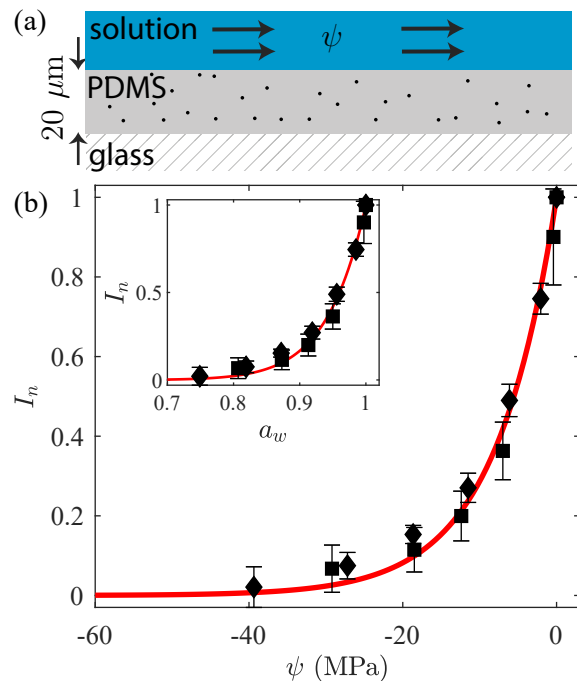


FIG. 5. (a) Sketch of the calibration experiment of the water clusters in PDMS. A solution at a given water potential ψ flows in a wide channel (height $\simeq 200 \mu\text{m}$, width $\simeq 1 \text{ mm}$) over a thin layer of PDMS bonded on a glass slide ($\simeq 20 \mu\text{m}$). The drawing shows only the bottom PDMS layer. (b) Relative normalized intensity I_n against ψ for glycerol solution (\blacklozenge) and NaCl solutions (\blacksquare). The red curve is a fit by eqn (3) with $\psi_c \simeq -8 \text{ MPa}$. Errorbars show the standard deviations based on data from eight different water clusters. Inset: same data against the corresponding water activity $a_w = \exp[V_m \psi / (RT)]$.

the normalized intensity I_n can roughly be fitted by:

$$I_n = \exp(-\psi/\psi_c), \quad (3)$$

with $\psi_c \simeq -8 \text{ MPa}$. This range of water potentials and of corresponding water activity a_w is consistent with the observations of Harley et al.⁴² that have reported a drastic increase of the water solubility in Sylgard-184 PDMS for vapour activity $\text{RH} > 0.7\text{--}0.8$. As noted by Harley et al.⁴², the exact mechanism for the water clustering around the hydrophilic sites, and its dependence with the water potential remain unknown. This mechanism could be similar to the osmotic pumping mechanism that has been proposed to explain the high water uptake of vulcanized rubbers, which is also due to the clustering of water molecules around hydrophilic impurities^{46,47}. However, the origin of an osmotic force induced by the hydration of fillers in Sylgard-184 remains to be demonstrated, and the role of the PDMS elastomer elasticity remains to be investigated.

C. Local estimates of the water potential

In the following, we exploit these clusters as sensors of the water potential in the PDMS matrix. Fig. 6 shows several snapshots zooming at the end of the evaporation zone, $x = 0$,

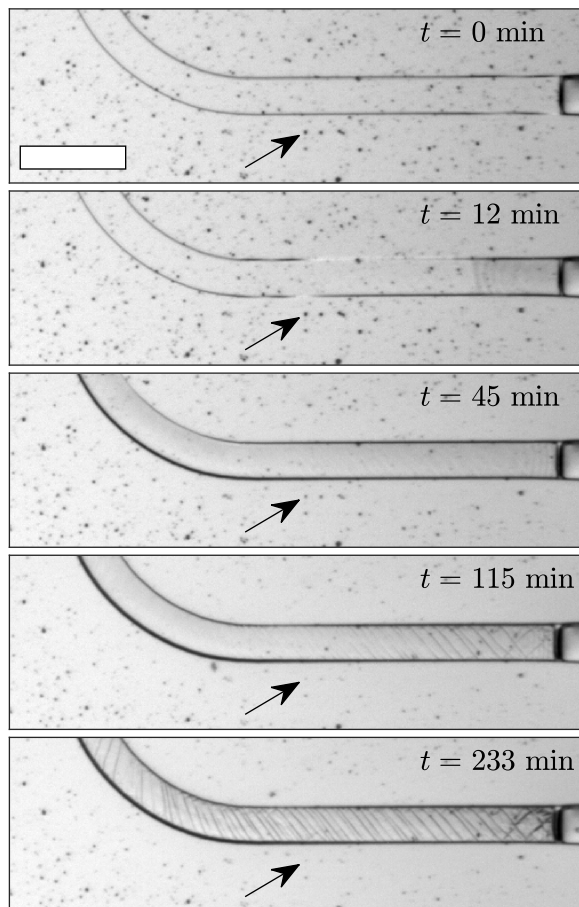


FIG. 6. Snapshots at different times t zooming in on the beginning of the serpentine channel, see also movie M3.avi †. Arrows point to a water cluster that disappears at $t \simeq 100$ min. The scale bar is equal to $300 \mu\text{m}$. The change of the texture of the solid at its end for $t \gtrsim 100$ min reveals the shear bands initially present, and suggests the invasion of air/water nanomenisci, see Section III E.

evidencing the growth of the colloidal solid at initial times. These images also reveal that some of the initially visible inclusions near the channel disappear over time, as the solid invades the channel. To better quantify this effect, we have selected 14 water clusters that disappear with time, located very close to the channel and with positions along the channel ranging from $x_i = 0.2$ to 3 mm, see the colored circles in Fig. 2. As for the calibration shown in Fig. 5, we have calculated the normalized intensity I_n measured by the camera for each water cluster, see Fig. 7. This plot clearly evidences a front of disappearance of these inclusions, parallel to the progression of the porous solid in the channel.

In order to make a rough estimate of the water potential at the locations of these different clusters, these curves are converted into water potential using eqn (3) and plotted against $x_c - x_i$, see the inset of Fig. 7. These data unambiguously show that the water potential in the vicinity of the microfluidic channel at a position x_i decreases over time as the colloidal solid grows beyond this position in the channel (i.e., when $x_c - x_i > 0$). In the following, we will use these data

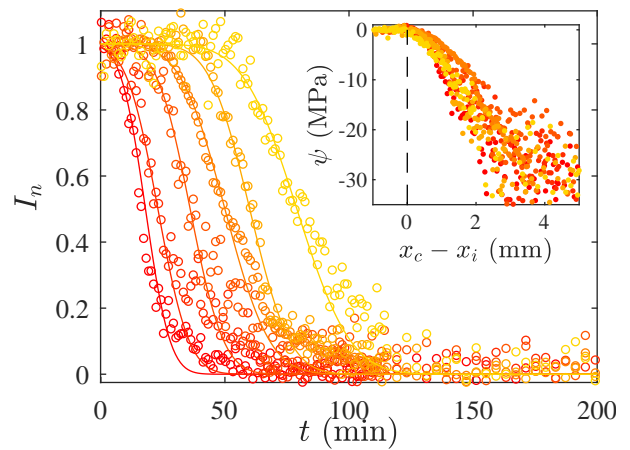


FIG. 7. Relative normalized intensity I_n against time t for the water clusters shown in Fig. 2. Only 6 curves are shown for the sake of clarity, and the color gradient indicates the increasing positions x_i of the clusters along the channel (from $x_i \simeq 0.2$ to 3 mm). The continuous lines are guides for the eye. Inset: Corresponding water potential ψ using the calibration given by eqn (3) with $\psi_c = -8$ MPa, vs $x_c - x_i$ for the positions x_i shown in the main graph.

to estimate the water potential ψ at the different positions x_i along the channel.

D. Model

We now present a simplified model of the directional drying in our experiments. Fig. 8a shows a schematic view along the channel of the growth of the porous solid at a given time t . In this picture, we do not consider the concentrated layer of unconsolidated colloids upstream the compaction front ($x > x_c$) even if the later can extend over large scales due to collective diffusion in such charge-stabilized dispersions^{17,39}. The observed delamination implies that the solid has a smaller cross-section than the channel cross-section ($h \times w$). In the following, we neglect the small shrinkage of the solid across its width (a few microns for $w = 100 \mu\text{m}$) and we assume that most of the shrinkage occurs across the height as also observed in ref.¹¹ and¹². This is mainly due to the relative high aspect ratio of the channel ($h \times w = 30 \times 100 \mu\text{m}^2$) and the small thickness of the PDMS chip ($H = 200 \mu\text{m}$).

In the configuration sketched in Fig. 8, the colloid mass balance is:

$$(h_d \varphi_d - h \varphi_0) \frac{dx_c}{dt} \simeq h \varphi_0 J, \quad (4)$$

φ_d being the volume fraction of the porous solid, and h_d its thickness, both assumed constant. This relation can be derived strictly from convection-diffusion models⁴⁰ (see also ref.²⁴ discussing its validity for a non constant evaporation rate), and includes the variation of height $h \rightarrow h_d$ at the compaction front. This relation is consistent with the linear relationship observed between the compaction front x_c and the position of

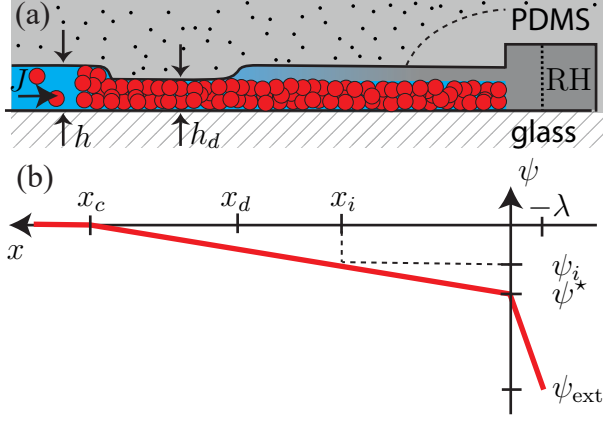


FIG. 8. (a) Schematic view of the transverse section along the serpentine channel showing both the compaction and delamination fronts at a given time t (not to the scale). The dotted line shows the cluster-free region in PDMS (black dots), where the water potential $\psi \ll \psi_c = -8$ MPa. (b) Corresponding profile ψ vs x at time t . x_i shows the position of a given cluster and its water potential ψ_i . $\psi_{\text{ext}} = RT/V_m \log(\text{RH})$ is the water potential in the air stream of imposed relative humidity RH, and $\psi^* = \psi(x=0)$.

the meniscus x_m , see Fig. 3b and eqn (2). As shown by Lesaine et al. using precise dry extract measurements^{48,49}, the volume fraction of dried layers of similar Ludox dispersions is $\phi_d \simeq 0.64$ for evaporation rates larger than $\dot{E} \geq 10$ nm/s. Values close to $\phi_d \simeq 0.64$ have also been measured using in situ small-angle X-ray scattering on similar nanosilica dispersions drying in similar configurations^{8,50}. In the following, we thus assume the same value, and the linear fit shown in Fig. 3b along with eqn (4) leads to $h_d/h \simeq 0.82$. This value corresponds to a thickness of $\simeq 5$ μm for the air gap shown in Fig. 8a, and is consistent with observations at high magnifications of the dried solid across its height (data not shown).

Estimating the rate of evaporation in the configuration shown in Fig. 8 a priori requires a three-dimensional model taking into account both the transport of the water vapour in the air gap downstream of the delamination front ($x < x_d$) and the transport of liquid water through the porous solid ($x < x_c$). For this model, we follow an approach similar to that used in ref.²⁸ and²⁴ based on the use of the water potential ψ as it allows to describe water independently of its state: liquid in the dispersion and in the porous solid, to vapor in the gas phase. We also assume local thermodynamic equilibrium and quasi-static conditions, i.e., continuity of the water potential. We also consider a porous solid fully saturated with water, and we do not initially consider the role played by cracks, see below for a discussion.

The mass flux of liquid water J_l^m ($\text{kg m}^{-2} \text{s}^{-1}$) through the colloidal solid is driven by gradients of water potential and described by the Darcy's law:

$$J_l^m = -\rho_w \frac{\kappa}{\eta_w} \nabla \psi, \quad (5)$$

with κ the permeability of the solid, and η_w (Pa s) the viscosity of water. In the gas phase, the mass flux of water J_g^m

($\text{kg m}^{-2} \text{s}^{-1}$) is driven by gradients of water vapour concentration c_w (kg m^{-3}), and given by:

$$J_g^m = -D_w^{\text{air}} \nabla c_w. \quad (6)$$

This relationship can be rewritten using the definition of the water potential in the gas phase:

$$\psi = \frac{RT}{V_m} \log \left(\frac{c_w}{c_{\text{sat}}} \right), \quad (7)$$

leading to:

$$J_g^m = -D_w^{\text{air}} c_{\text{sat}} \frac{V_m}{RT} \exp \left(\frac{V_m \psi}{RT} \right) \nabla \psi. \quad (8)$$

Continuity for the fluid flow (assuming constant density ρ_w) and quasi-static conditions in the gas phase imposes $\text{div}(J_l^m) = 0$ and $\text{div}(J_g^m) = 0$ respectively, and thus:

$$\nabla \cdot \left[-\rho_w \frac{\kappa}{\eta_w} \nabla \psi \right] = 0, \quad (9)$$

$$\nabla \cdot \left[-D_w^{\text{air}} c_{\text{sat}} \frac{V_m}{RT} \exp \left(\frac{V_m \psi}{RT} \right) \nabla \psi \right] = 0. \quad (10)$$

Eqn (9) and (10) can be seen as two steady state diffusion equations for the water potential ψ with the effective diffusion coefficients, $\rho_w \kappa / \eta_w$ for the liquid phase and $D_w^{\text{air}} c_{\text{sat}} \frac{V_m}{RT} \exp \left(\frac{V_m \psi}{RT} \right)$ for the vapour phase, the latter being a function of ψ . Boundary conditions for these equations are given by $\psi(x_c, t) = 0$ (the liquid dispersion, neglecting the osmotic contribution of the unconsolidated colloids upstream the compaction front), $\psi(-\lambda, t) = \psi_{\text{ext}} = RT/V_m \log(\text{RH})$ (imposed relative humidity in the air stream), and impermeability on the glass slide $\nabla \psi \cdot \mathbf{n} = 0$. The boundary condition on the PDMS walls is less obvious as the PDMS matrix is itself permeable to water. We will assume for simplicity that the transport in the PDMS matrix is negligible, and that the PDMS walls are almost impermeable (see Section III F for a discussion of this approximation). Eqn (9) and (10) along with the boundary conditions given above can be solved numerically for a given geometric configuration, such as the one shown schematically in Fig. 8a. Such a numerical resolution should then lead to the mass fluxes given by eqn (5) and (8), and thus to the global evaporation rate J . Nevertheless, we show below using simple theoretical arguments that the vapour transport through the air gap is negligible, and that the evaporation rate J can be described by a simple one-dimensional equation.

The ratio of the two effective diffusion coefficients in eqn (9) and (10) is given by:

$$\varepsilon = \left(\frac{D_w^{\text{air}} c_{\text{sat}} V_m}{RT} \right) \exp \left(\frac{V_m \psi}{RT} \right) / \left(\frac{\rho_w \kappa}{\eta_w} \right). \quad (11)$$

This ratio compares the mass flux of water through the gas phase with that through the porous solid for a given water potential gradient. Assuming that the permeability κ of the solid is correctly described by the Carman-Kozeny relation⁵¹:

$$\kappa_{CK} = \frac{(1 - \phi_d)^3}{45 \phi_d^2} a^2, \quad (12)$$

$\kappa_{CK} = 3.1 \times 10^{-19} \text{ m}^2$, $\varepsilon \ll 1$ even for high water potential ($\psi = 0$). Furthermore, the aspect ratio h/x_d in the geometry shown in Fig. 8a is extremely small and the water potential is therefore approximately uniform over the channel cross-section, i.e., $\psi \simeq \psi(x, t)$. Because $\varepsilon \ll 1$, the mass flux of liquid water through the porous solid is much higher than the water mass flux in air, and the global mass balance imposes $(hw)\rho_w J \simeq (h_d w)J_i^m$. Eqn (5) then shows that the water potential decreases linearly along the channel following the Darcy's law:

$$\psi(x, t) \simeq \frac{h}{h_d} \frac{\eta_w J}{\kappa} [x - x_c(t)], \quad (13)$$

as if the air gap due to delamination was not playing a role (negligible transport through the gas phase). This linear decrease is shown schematically in Fig. 8b. This assumption is also found in work on confined directional drying^{6,7}, which implicitly assumes that the gas phase in the cracks and air films due to delamination is in equilibrium with the liquid phase inside the porous solid. It should be noted, however, that vapor in equilibrium in the air gap may have a humidity RH significantly smaller than 1, due to the potentially low water potential values, see Section III E.

The simplified model presented above does not take into account the cracks observed in the porous solid, see Fig. 2. Yet these cracks literally cut the solid into several pieces, calling into question the description of a continuous liquid flow as described by Darcy's law, eqn (5). Nevertheless, it is quite conceivable that water is transported through the vapour phase between the different solid pieces. As the thickness ξ of the cracks is very small compared to x_c , $\xi \simeq 20\text{--}40 \text{ }\mu\text{m}$, eqn (9) and (10) can be used to show that the resistance added by the cracks is negligible despite the fact that $\varepsilon \ll 1$. This confirms the continuous description of eqn (13) and also probably explains why the appearance of cracks does not significantly affect the dynamics of both the compaction front x_c and the evaporation rate J in our experiments, see Fig. 3.

E. Application to experiments

As demonstrated in Section III C, the water clusters in PDMS allow a rough estimate of the water potential at their location x_i along the channel, see the inset of Fig. 7. The clusters chosen in Fig. 2 are located very close to the side walls of the channel, so we can assume they give good estimates of the water potential in the channel at $x = x_i$. As described above, the water potential profile decreases linearly along the channel from $\psi(x_c, t) = 0$, see eqn (13), so that we can estimate the permeability κ from the measured values $\psi(x_i, t)$ at the different clusters using:

$$\kappa = \frac{h}{h_d} \frac{\eta_w J}{\psi(x_i, t)} [x_i - x_c(t)]. \quad (14)$$

In order to eliminate the noise associated with very small values of water potential and $x_i - x_c$, we have only considered data from the inset in Fig. 7 ranging from $\psi(x_i, t) = -25$ to

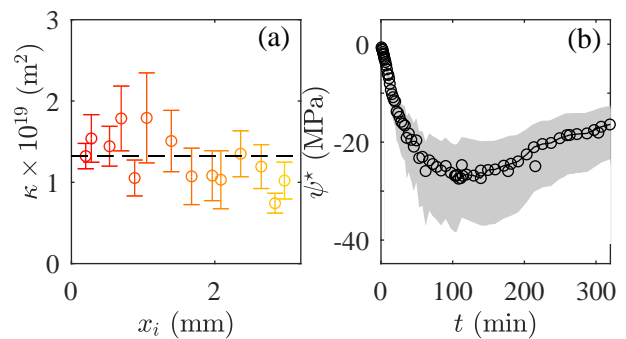


FIG. 9. (a) Permeability values κ estimated from eqn (14) as a function of the position x_i of the chosen cluster (see color code in Fig. 2). The errorbars are calculated from the standard deviation estimated for each cluster. (b) Estimated water potential ψ^* at $x = 0$ using eqn (15) and $\kappa \simeq 1.3 \times 10^{-19} \text{ m}^2$ (○). The shaded area corresponds to the same estimates but with a difference of $\pm 0.4 \times 10^{-19} \text{ m}^2$ for κ .

–5 MPa to estimate κ using eqn (14) and the data on evaporation rate J and compaction front x_c shown in Fig. 3. This analysis leads to the κ values shown in Fig. 9a. Despite the dispersion, no trend is observed in the permeability estimate, neither with the position x_i of the different clusters, nor with the time t for a given cluster (not shown). Moreover, we found the same trends and values for another experiment carried out under the same conditions, and it allows us to reasonably confirm that $\kappa \simeq 1.3 \pm 0.4 \times 10^{-19} \text{ m}^2$. This permeability value is slightly smaller than the one estimated by the Carman-Kozeny relation, $\kappa \simeq 0.4 \kappa_{CK}$, possibly due to the polydispersity of the nanoparticles. It is worth mentioning that this lower value of permeability does not affect the hypothesis formulated above for the ratio of the two effective diffusion coefficients given in eqn (11), as $\varepsilon \ll 1$ even for this value of κ .

Fig. 9b finally shows the extrapolated water potential at $x = 0$:

$$\psi^* = -\frac{h}{h_d} \frac{\eta_w J}{\kappa} x_c, \quad (15)$$

assuming $\kappa = 1.3 \times 10^{-19} \text{ m}^2$. Lidon et al. have also reported similar measurements of the product Jx_c versus t for similar dispersions²⁵, see eqn (15), but we go here a step further with our measurements of κ enabling us to estimate the water potential at $x = 0$. ψ^* first decreases and reaches a plateau for $t \gtrsim 80$ min around $\psi^* \simeq -27$ MPa, and then slightly grows for $t \gtrsim 150$ min up to $\psi^* \simeq -17$ MPa at $t \simeq 320$ min. The plateau observed for $t \gtrsim 80$ min coincides with the transition between the linear growth rate for the compaction front, $x_c \sim t$, and the slowdown observed on longer time scales, see Fig. 3a.

Also, this transition almost coincides with an apparent change of the texture of the solid material at its end, see the snapshots in Fig. 6, and movie M3.avi †. For $t \gtrsim 100$ min, the texture of the porous solid around $x = 0$ loses its homogeneity, thus increasing the contrast of the shear bands, which were barely visible at shorter times^{9,10}. All these observations suggest that the value $\psi^* \simeq -27$ MPa, much larger than the water potential imposed in the air stream $\psi_{\text{ext}} \simeq -220$ MPa,

actually corresponds to the capillary pressure ψ_{cap} at which air/water nanomenisci invade the porous solid, leading to a higher optical contrast. It is traditionally assumed that this air invasion adds a resistance to the water mass transfer, therefore slowing down the evaporation rate^{7,24}. Our quantitative estimate, $\psi_{\text{cap}} \simeq -27$ MPa (with a range of confidence from -37 to -20 MPa because of the uncertainty on κ , see Fig. 9b) made possible thanks to our measurements of κ , is roughly consistent with standard estimates given by $\psi_{\text{cap}} = -\alpha\gamma/a$, with α a geometrical prefactor which, according to studies, leads to predictions ranging from $\psi_{\text{cap}} \simeq -35$ MPa as in ref.²⁴ to $\psi_{\text{cap}} = -85$ MPa as in ref.⁶.

F. Discussions

As soon as air invades the porous solid, the description presented in Fig. 8 is no longer valid, as an additional resistance must be taken into account because of the transport of the vapour by diffusion across a dry layer of solid. In particular, the extrapolated values of ψ^* using eqn (15) are no longer valid either, and our model cannot therefore interpret the rise in ψ^* observed at long times in Fig. 9b ($t > 150$ min). In this *capillary-limited regime*, i.e., $\psi_{\text{cap}} > \psi_{\text{ext}}$, the quantitative prediction of the evaporation rate remains an open question. All theoretical works^{24–26} consider a one-dimensional description of directional drying. These models suggest that desaturation takes place from the tip of the solid at $x = 0$, and over a very small length due to the strong resistance to mass transfer by vapour diffusion through the porous dry layer. The change of the texture of the solid at long times shown in Fig. 6 suggests that the invasion of the nanomenisci occurs over a long length scale within the channel, possibly leading to the progressive desaturation of the porous solid across its height. These observations challenge the theoretical work cited above and call for new models and experimental measurements.

Finally, throughout our approach, we have assumed that the channel walls are impermeable to water, but there may also be water transfer through the PDMS matrix. Considering typical values for water solubility and water diffusion coefficient in PDMS⁴², it is easy to show using a similar approach leading to eqn (9) and (10) that the associated mass transfer resistance is very high, supporting our simplification. However, it is possible that mass transfer through the PDMS matrix plays a role at long times, when the driving force of evaporation along the channel becomes weaker and weaker ($J \rightarrow 0$). Indeed, the water bath imposes a water potential $\psi = 0$ at the top of the PDMS layer embedding the channel (thickness $H = 200$ μm , see Fig. 1). This implies that there is a minute flux of water from the bath towards the channel, as soon as $\psi(x, t) < 0$ in the channel. This flux could possibly explain the over-slowdown observed for the compaction front at long times ($x_c \sim t^{0.4}$), because it further reduces the driving force of evaporation within the channel. All these considerations call for advanced, three-dimensional modeling of mass transfer in this type of experiment to confirm these assumptions.

IV. CONCLUSIONS AND OUTLOOKS

The model described in the previous sections, correlated with original measurements of the water potential, has enabled us to estimate both the Darcy permeability κ and capillary pressure ψ_{cap} of the porous solid made of silica nanoparticles. We are not aware of any measurements of these two quantities by other independent techniques for comparison, but the measured values are consistent with the theoretical predictions. Our experimental measurements open up a number of possibilities, in particular for the quantitative description of drying-induced stresses, as the value of κ plays a fundamental role in poro-elastic modeling^{40,52–54}. In our experiments for instance, the knowledge of κ enables us to estimate the water potential ψ , and therefore the pore pressure within the solid, a quantity related to the tensile component of the stresses during drying^{40,53,54}. The data shown in the inset of Fig. 9 correlated with the observations gathered in Fig. 3 can then be used to link the value of the pore pressure to the various observed instabilities: shear bands, delamination, and cracks.

The quantitative description of confined directional drying presented in this work was made possible by original, but approximate, measurements of the water potential using (uncontrolled) hydrophilic sites within the PDMS matrix. Such observations have rarely been reported in the literature (in particular, the data in Fig. 4 and 5) and open up numerous perspectives that go well beyond the study of this work. We believe it is essential to better understand these phenomena, and even to use calibrated inclusions for more precise and controlled measurements of the water potential, because the significantly large errorbars of the calibration curve shown in Fig. 5 are likely due to the polydispersity of the water clusters evidenced in our work. This approach shares strong similarities with the methods developed by Jain et al. based on fluorescent nanogels in order to probe in situ water potential in plant leaves with high precision⁵⁵. It seems to us that these innovative approaches could also open up many new prospects for understanding drying of colloidal dispersions.

CONFLICTS OF INTEREST

There are no conflicts to declare.

ACKNOWLEDGEMENTS

We acknowledge Solvay, CNRS and the ANR program grant no. ANR-18-CE06-0021 for financial support.

¹W. B. Russel, *AIChE*, 2011, **57**, 1378.

²A. F. Routh, *Rep. Prog. Phys.*, 2013, **76**, 046603.

³L. Goehring, A. Nakahara, T. Dutta, S. Kitsunozaki and S. Tarafdar, *Desiccation Cracks and their Patterns*, Wiley-VCH Verlag GmbH & Co. KGaA, 2015.

⁴P. Bacchin, D. Brutin, A. Davaille, E. Di Giuseppe, X. D. Chen, I. Gergianakis, F. Giorgiutti-Dauphiné, L. Goehring, Y. Hallez, R. Heyd and et al., *Eur. Phys. J. E*, 2018, **41**, 94.

⁵C. Allain and L. Limat, *Phys. Rev. Lett.*, 1995, **74**, 2981.

- ⁶E. R. Dufresne, E. I. Corwin, N. A. Greenblatt, J. Ashmore, D. Y. Wang, A. D. Dinsmore, J. X. Cheng, X. Xie, J. W. Hutchinson and D. A. Weitz, *Phys. Rev. Lett.*, 2003, **91**, 224501.
- ⁷E. R. Dufresne, D. J. Stark, N. A. Greenblatt, J. X. Cheng, J. W. Hutchinson, L. Mahadevan and D. A. Weitz, *Langmuir*, 2006, **22**, 7144.
- ⁸F. Boulogne, L. Pauchard, F. Giorgiutti-Dauphiné, R. Botet, R. Schweins, M. Sztucki, J. Li, B. Cabane and L. Goehring, *Europhys. Lett.*, 2014, **105**, 38005.
- ⁹P. Kiatkirakajorn and L. Goehring, *Phys. Rev. Lett.*, 2015, **115**, 088302.
- ¹⁰B. Yang, J. S. Sharp and M. I. Smith, *ACS Nano*, 2015, **9**, 4077.
- ¹¹A. Sarkar and M. S. Tirumkudulu, *Soft Matter*, 2011, **7**, 8816.
- ¹²Y. Xu, W. Engl, E. R. Jerison, K. J. Wallenstein, C. Hyland, L. A. Wilen and E. R. Dufresne, *Proc. Natl. Acad. Sci. USA*, 2010, **107**, 14964.
- ¹³G. Gauthier, V. Lazarus and L. Pauchard, *Langmuir*, 2007, **23**, 4715.
- ¹⁴S. Inasawa and Y. Yamaguchi, *Soft Matter*, 2012, **8**, 2416.
- ¹⁵Y. Xu, G. K. German, A. F. Mertz and E. R. Dufresne, *Soft Matter*, 2013, **9**, 3735.
- ¹⁶A. Sarkar and M. S. Tirumkudulu, *Langmuir*, 2009, **25**, 4945.
- ¹⁷L. Goehring, J. Li and P.-C. Kiatkirakajorn, *Phil. Trans. R. Soc. A*, 2017, **375**, 20160161.
- ¹⁸K. Inoue and S. Inasawa, *RSC Adv.*, 2020, **10**, 15763.
- ¹⁹E. Hooiveld, H. M. van der Kooij, M. Kisters, T. E. Kodger, J. Sprakel and J. van der Gucht, *J. Colloid Interface Sci.*, 2023, **630**, 666.
- ²⁰C. Noirjean, M. Marcellini, S. Deville, T. E. Kodger and C. Monteux, *Phys. Rev. Mater.*, 2017, **1**, 065601.
- ²¹S. Inasawa, Y. Oshimi and H. Kamiya, *Soft Matter*, 2016, **12**, 6851.
- ²²E. Keita, P. Faure, S. Rodts and P. Coussot, *Phys. Rev. E*, 2013, **87**, 62303.
- ²³E. Ghiringhelli, M. Marcoux, S. Geoffroy and M. Prat, *Colloids and Surfaces A*, 2023, **656**, 130432.
- ²⁴H. Pingulkar and J. B. Salmon, *Soft Matter*, 2023, **19**, 2176.
- ²⁵P. Lidon and J.-B. Salmon, *Soft Matter*, 2014, **10**, 4151.
- ²⁶K. J. Wallenstein and W. B. Russel, *J. Phys.: Condens. Matter*, 2011, **23**, 194104.
- ²⁷J. Thiery, S. Rodts, D. A. Weitz and P. Coussot, *Phys. Rev. Fluids*, 2017, **2**, 074201.
- ²⁸O. Vincent, A. Szenicer and A. D. Stroock, *Soft Matter*, 2016, **12**, 6656.
- ²⁹E. Choi, H. K. Chang, C. Y. Lim, T. Kim and J. Park, *Lab Chip*, 2012, **12**, 3968.
- ³⁰E. Choi, K. Kwon, D. Kim and J. Park, *Lab Chip*, 2015, **15**, 168.
- ³¹N. Goedecke, J. Eijkel and A. Manz, *Lab Chip*, 2002, **2**, 219.
- ³²V. Namasivayam, R. G. Larson, D. T. Burke and M. A. Burns, *J. Microech. Microeng.*, 2003, **13**, 261.
- ³³P. Bacchin, J. Leng and J. B. Salmon, *Chem. Rev.*, 2022, **122**, 6938.
- ³⁴W. J. Massman, *Atmos. Environ.*, 1998, **32**, 1111.
- ³⁵G. C. Randall and P. S. Doyle, *Proc. Natl. Acad. Sci. USA*, 2005, **102**, 10813.
- ³⁶E. Verneuil, A. Buguin and P. Silberzan, *Europhys. Lett.*, 2004, **68**, 412.
- ³⁷B. Dollet, J.-F. Louf, M. Alonzo, K. Jensen and P. Marmottant, *J. R. Soc. Interface*, 2019, **16**, 20180690.
- ³⁸X. Noblin, L. Mahadevan, I. A. Coomaraswamy, D. A. Weitz, N. M. Holbrook and M. A. Zwierniecki, *Proc. Natl. Acad. Sci. USA*, 2008, **105**, 9140.
- ³⁹B. Sobac, S. Dehaeck, A. Bouchaudy and J.-B. Salmon, *Soft Matter*, 2020, **16**, 8213.
- ⁴⁰R. W. Style and S. S. Peppin, *Proc. R. Soc. A*, 2011, **467**, 174.
- ⁴¹J. M. Watson and M. G. Baron, *J. Membr. Sci.*, 1996, **110**, 47.
- ⁴²S. J. Harley, E. A. Glascoe and R. S. Maxwell, *J. Phys. Chem. B*, 2012, **116**, 14183.
- ⁴³A. J. Fontana, in *Water Activity in Foods*, Wiley, 2007, p. 395.
- ⁴⁴L. Ninni, M. S. Camargo and A. J. A. Meirelles, *J. Chem. Eng. Data*, 2000, **45**, 654.
- ⁴⁵A. Bouchaudy, C. Loussert and J.-B. Salmon, *AIChE*, 2018, **64**, 358.
- ⁴⁶R. Fedors, *Polymer*, 1980, **21**, 207.
- ⁴⁷A. Thomas and K. Muniandy, *Polymer*, 1987, **28**, 408.
- ⁴⁸K. Piroird, V. Lazarus, G. Gauthier, A. Lesaine, D. Bonamy and C. Rountree, *Europhys. Lett.*, 2016, **113**, 38002.
- ⁴⁹A. Lesaine, D. Bonamy, C. L. Rountree, G. Gauthier, M. Impéror-Clerc and V. Lazarus, *Soft Matter*, 2021, **17**, 1589.
- ⁵⁰B. Yang, N. D. Smith, A. Johannes, M. Burghammer and M. Smith, *Sci. Rep.*, 2018, **8**, 12979.
- ⁵¹B. J. Rogers and M. J. Wirth, *ACS Nano*, 2013, **7**, 725.
- ⁵²M. Chekchaki and V. Lazarus, *Transp Porous Med.*, 2013, **100**, 143.
- ⁵³A. Bouchaudy and J.-B. Salmon, *Soft Matter*, 2019, **15**, 2768.
- ⁵⁴M. G. Hennessy, R. V. Craster and O. K. Matar, *Phys. Rev. E*, 2022, **105**, 1.
- ⁵⁵P. Jain, W. Liu, S. Zhu, C. Y. Y. Chang, J. Melkonian, F. E. Rockwell, D. Pauli, Y. Sun, W. R. Zipfel, N. Michele Holbrook, S. J. Riha, M. A. Gore and A. D. Stroock, *Proc. Natl. Acad. Sci. USA*, 2021, **118**, 1.